CrossMark

High power TiO$_2$ and high capacity Sn-doped TiO$_2$ nanomaterial anodes for lithium-ion batteries

Mechthild Lübke [a], Ian Johnson [a], Neel M. Makwana [a], Dan Brett [b], Paul Shearing [b], Zhaolin Liu [c], Jawwad A. Darr [a, *, 1]

[a] Department of Chemistry, University College London, 20 Gordon Street, London, WC1H 0AJ, UK
[b] Department of Chemical Engineering, University College London, Torrington Place, London, WC1E 7JE, UK
[c] Institute of Materials Research and Engineering, Agency for Science, Technology and Research (A*STAR), 3 Research Link, Singapore 117602, Singapore

HIGHLIGHTS

- Phase-pure and Sn-doped TiO$_2$ nanoparticles (<7 nm) are synthesized via CHFS.
- The nanomaterial can be used directly after synthesis as a Li-ion battery anode.
- TiO$_2$ retains excellent high power performance at current rates up to 10 A g^{-1}.
- Doped Sn^{4+} in the TiO$_2$ is electrochemically active.

ARTICLE INFO

ABSTRACT

A range of phase-pure anatase TiO$_2$ (~5 nm) and Sn-doped TiO$_2$ nanoparticles with the formula Ti$_{1-x}$Sn$_x$O$_2$ (where x = 0, 0.06, 0.11 and 0.15) were synthesized using a continuous hydrothermal flow synthesis (CHFS) reactor. Charge/discharge cycling tests were carried out in two different potential ranges of 3 to 1 V and also a wider range of 3 to 0.05 V vs Li/Li$^+$. In the narrower potential range, the undoped TiO$_2$ nanoparticles display superior electrochemical performance to all the Sn-doped titania crystallites. In the wider potential range, the Sn-doped samples perform better than undoped TiO$_2$. The sample with composition Ti$_{0.85}$Sn$_{0.15}$O$_2$, shows a capacity of ca. 350 mAh g^{-1} at an applied constant current of 100 mA g^{-1} and a capacity of 192.3 mAh g^{-1} at a current rate of 1500 mA g^{-1}. After 500 charge/discharge cycles (at a high constant current rate of 382 mA g^{-1}), the same nanomaterial anode retains a relatively high specific capacity of 240 mAh g^{-1}. The performance of these nanomaterials is notable, particularly as they are processed into electrodes, directly from the CHFS process (after drying) without any post-synthesis heat-treatment, and they are made without any conductive surface coating.

1. Introduction

Continued interest in high performance lithium-ion batteries has driven the development of new electrode materials and their synthesis techniques, often targeting scalable production of high quality nanoceramics (<100 nm in diameter), which may offer performance improvements. However, there are a number of hurdles, which need to be overcome to move away from current batch synthesis methods that offer poor reproducibility or lack of control over crystallite attributes, particularly at larger scale syntheses.

Continuous hydrothermal flow synthesis (CHFS) processes are a promising route for the direct and controlled manufacture of Li-ion battery electrode nanoceramics. Such processes use superheated water and metal salt mixtures as reagents. In a typical CHFS reaction, a feed of supercritical water (above the critical point of water (T_C = 374 °C and P_c = 22.1 MPa), is rapidly mixed in an engineered mixer [1] with a metal salt/base aqueous precursor feed (at ambient temperature and the same pressure), resulting in rapid formation of the corresponding nanocrystallite oxide in the water. This nucleation dominated reaction occurs as a result of the metal salts being supersaturated upon mixing with sc-water and also instantly being

hydrolysed and dehydrated under these exotic reaction conditions. The nascent nanocrystallite metal oxide stream in water is then cooled in process and then can be constantly collected from the exit of the CHFS process as an aqueous nanoparticle slurry at ambient temperature. The cleaned crystallites (e.g. via dialysis) can be obtained as a wet solid and then freeze-dried to retain maximum surface area and reduce agglomeration.

Compared to batch hydrothermal syntheses, CHFS type processes typically produce very small nanoparticles (<10 nm) with a narrow size distribution [2–4]. Additionally, CHFS processes are highly scalable (>1 kg per hour in the lab of the UCL authors [5]) and can be used to make high quality nanoparticles at scale, with little or no significant variation between those made on the smaller CHFS laboratory scale process. The general CHFS reactor design used by the authors for the synthesized nanomaterials herein, is presented in Fig. 1 [1,5–8].

A typical lithium-ion battery consists of an anode and cathode, separated by a separator soaked with a lithium-ion salt containing electrolyte. One approach to increase the specific capacity and the cycle life of Li-ion batteries is nanosizing the electrode materials, because this can not only improve conductivity, but can also facilitate faster Li ion diffusion due to a greater portion of Li being closer to the surface in nanomaterials [9,10]. There are currently many candidates for anode materials for lithium-ion batteries. Insertion materials such as titanium oxides, offer good sustainability, low cost, low risk to the environment, high cell safety, low capacity loss, high power capability and a very high cycle life due to minimal volume and structural changes during cycling. Furthermore, such materials have a narrower operational potential window, which can decrease specific energy [11,12].

Alternative Li-ion anode materials such as alloys, show far higher theoretical capacities (e.g. Si = 4200 mAh g^{-1}, Sn = 993 mAh g^{-1}, and SnO$_2$ = 793 mAh g^{-1} [13]) compared to insertion materials (e.g. TiO$_2$ = 335 mAh g^{-1} and LTO = 175 mAh g^{-1} [14]). The higher capacities and the wider operating potential windows of such alloys, result in higher energy densities, however, they can also show large irreversible capacity losses during the initial cycles and high

capacity fading (poor cycle life) due to the tremendous volume changes (and subsequent deleterious structural changes) in the electrode during each lithiation and delithiation cycle (e.g. >200% volume change for Sn alloys [15]).

Herein, the authors investigated the influence of Sn doping in nanosized anatase TiO$_2$ on the rate performance and specific capacity at different current rates (in two different potential ranges). The doped titanias were investigated in the potential ranges of 1–3 V vs Li/Li$^+$ and 0.05–3 V vs Li/Li$^+$, respectively. Electrochemical results suggested that the high surface area (and small crystallite size) played a crucial role on the rate capability when cycling between 1 and 3 V vs Li/Li$^+$. The results also suggest that at potentials below 1 V vs Li/Li$^+$, the doped Sn became an electrochemically active component, resulting in higher capacities (and increased specific energy density) compared to undoped TiO$_2$. Compared to pure alloy materials such as SnO$_2$, which can suffer from low cycle stability, the Sn doped titania samples also showed excellent stability over 500 cycles.

2. Experimental section

2.1. Synthesis of nanoparticle anode materials

The nanoparticles were synthesised using a continuous hydrothermal flow synthesis (CHFS) reactor incorporating a patented confined jet mixer, the basic design of which is described elsewhere [1,2]. Briefly, the laboratory scale CHFS process is similar to the larger pilot plant CHFS process described elsewhere [5,16] but on ca. 1/5 of its scale. In the process, the metal salt precursor 1 (aq), which contained the tin and titanium salts in a single solution (flow rate = 40 mL min^{-1}) was premixed with the precursor 2, base KOH (flow rate = 40 mL min^{-1}) at room temperature in a dead volume tee piece and this combined base and metal feed was then brought into contact with a flow of supercritical water at ca. 400 °C and 24.1 MPa (flow rate = 80 mL min^{-1}) in a confined jet reactor, CJM (see Ref. [1]). The patented CJM was designed to mix the superheated water (inner annulus pipe of CJM) with the metal feed
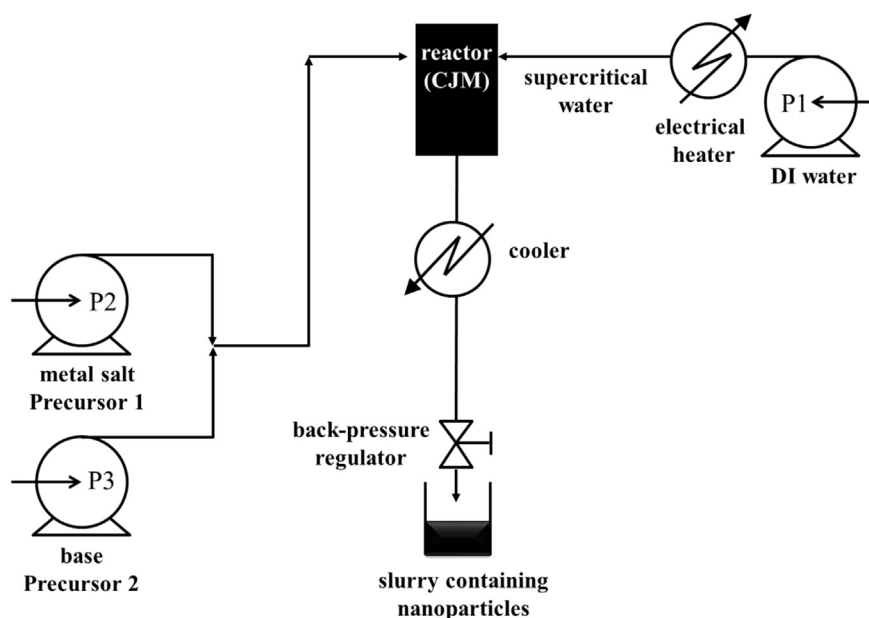

Fig. 1. CHFS reactor incorporating a confined jet mixer (CJM). The metal salt (pump P2, 40 mL min^{-1}) and base (pump P3, 40 mL min^{-1}) precursor are mixed together at room temperature and then combined in a supercritical water flow (pump P1, 80 mL min^{-1}) in the CJM. After cooling, the nanocrystallite slurry is constantly harvested from the exit of the back-pressure regulator.

(outer annulus) and eliminate blockages under these conditions and facilitate highly turbulent mixing if needed. The Reynolds number was calculated to be *ca.* 6565 and the residence time was *ca.* 5 sec, with a mixing temperature of 368 °C. For the metal salt feed, the precursor solution of a mixture of acidified titanium oxysulphate hydrate (TiOSO$_4$: 29 wt% TiO$_2$ and 17 wt% H$_2$SO$_4$, Sigma Aldrich, Steinheim, Germany) and tin(IV) sulphate (SnSO$_4$ 97%, Acros Organics, Geel, Belgium) were combined to give a total metal ion concentration of 0.0625 M. The titanium salt was used with a concentration of 0.0625, 0.06, 0.575 and 0.055 M, whereas for the last three concentrations, the tin salt concentration was set to 0.0025, 0.005 and 0.0075 M, respectively. These concentrations corresponded to a nominal precursor Sn at% of 0, 4, 8 and 12%, however, the samples were labelled according to actual at% of Sn measured via EDX, i.e. the actual formulas of TiO$_2$, Ti$_{0.94}$Sn$_{0.06}$O$_2$, Ti$_{0.89}$Sn$_{0.11}$O$_2$, Ti$_{0.85}$Sn$_{0.15}$O$_2$, i.e. corresponding to 0, 6, 11, and 15 at% Sn, respectively. The base concentration was kept constant throughout all experiments at 0.0703 M. At the end of the CHFS process, the solids in the nanoparticle laden slurry were cleaned by allowing them to settle before washing (three times) in DI water (10 MΩ) with shaking and then finally, the wet solids were freeze-dried (Virtis Genesis 35XL) at −60 °C for 24 h under vacuum of <100 mTorr. The as-prepared freeze-dried powders were used directly for the preparation of anode inks, with no further processing or treatments whatsoever.

2.2. Characterization

Powder X-ray diffraction (XRD) patterns of the samples were obtained on an STOE diffractometer using Mo-Kα radiation (λ = 0.71 Å), over the 2θ range 2–35° with a step size of 0.5° and step time of 20 s. X-ray photoelectron spectroscopy (XPS) measurements were collected using a Thermo Scientific™ K-alpha™+ spectrometer using Al-Kα radiation and a 128-channel position sensitive detector. Survey scans were conducted at an energy of 150 eV and high resolution region scans were conducted at 50 eV. The XPS spectra were processed using CasaXPS™ software (version 2.3.16). The binding energy scale was calibrated by a C 1s peak at 285.0 eV.

The size and morphology of the crystallites were determined by transmission electron microscopy (TEM) using a Jeol JEM 2100 − LaB$_6$ filament. The system was equipped with a Gatan Orius digital camera for digital image capturing. Samples were prepared by briefly ultrasonically dispersing a few mg of the powder in ethanol (>99.5%, EMPLURA, Darmstadt, Germany) and pipetting drops of the dispersed sample on to a copper film grid (300 mesh − Agar Scientific, Stansted, UK). The average crystallite size was determined by the average of at least 150 crystallites with ImageJ software. Brunauer−Emmett−Teller (BET) surface area measurements were carried out using N$_2$ in a micrometrics ASAP 2420 instrument. The samples were degassed at 150 °C (12 h) under vacuum before measurements.

2.3. Electrode preparation and electrochemical characterization

Sn-doped TiO$_2$ samples were used as the electrode active material without any further post-synthesis heat-treatment. The slurry for the electrode was prepared with a content of 70 wt% active material, 20 wt% conductive agent (carbon black, Super P, Alfa Aesar, Heysham, UK) and 10 wt% polyvinylidene fluoride, PVDF, (PI-KEM, Staffordshire, UK). PVDF was dissolved in NMP (N-Methyl-2-pyrrolidone, Sigma Aldrich, St. Louis, USA) for at least 1 h at room temperature, before adding the active material and conductive agent. The mixtures were milled and the slurry was cast on a copper foil (PI-KEM, Staffordshire, UK) and dried in an oven at 70 °C

for 1 h and then left overnight at room temperature. Electrodes with a diameter of 16 mm were punched out, pressed, and finally dried overnight at 70 °C. The electrodes had active material mass loadings in the range of *ca.* 1–4 mg cm^{-2}.

Electrochemical experiments were performed using a two-electrode 2032-type coin cell, which was assembled in an argon-filled glovebox with O$_2$ and H$_2$O limited below 50 ppm. The counter electrode was lithium metal foil (PI-KEM, Staffordshire, UK). The separator (glass microfiber filters, WHATMAN, Buckinghamshire, UK) was saturated with an organic electrolyte of LiPF$_6$ in 3:7 wt% ethylene carbonate/ethyl methyl carbonate (BASF, Ludwigshafen, Germany).

All electrochemical measurements were performed using a 48-channel Arbin Instrument (Caltest Instruments Ltd, Guildford, UK) at room temperature. The electrochemical performance was first investigated by CV (cyclic voltammetry) in the potential range 0.05−3 V vs Li/Li$^+$ with a scan rate of 0.05 mV s^{-1}. Galvanostatic charge/discharge cycling was also performed in the range 1−3 V and also in the range 0.05−3 V vs. Li/Li$^+$, applying a specific current during charge/discharge of 300 mA g^{-1} and 382 mA g^{-1}, respectively. The specific current rate test was performed in sequence for 10 scans each at 100, 200, 300, 500, 1000 and 1500 mA g^{-1}. For the pure TiO$_2$ electrode material, the specific current rates were increased up 10 A g^{-1} (i.e. 10,000 mA g^{-1}). The specific current and specific capacity was calculated based on the mass of active material in each printed electrode.

3. Results and discussion

The as-prepared pure nano-TiO$_2$ sample was collected as a white powder with a yield above 85%, whilst Sn doping changed the colour to light yellow. XRD data for all samples, suggested the presence of phase pure anatase TiO$_2$ [similar to JCPDS pattern 21−12729] for all samples. There were no additional peaks in the patterns (e.g. such as those for SnO$_2$ or other impurities), which was initially surprising given the high Sn loadings. It was observed (Fig. 2) (For interpretation of the references to colour in this figure legend, the reader is referred to the web version of this article) that upon doping, there was a slight shift in peak positions (~0.1°) towards lower angles, e.g. (004), (200), (204) and (215), which can be explained with the slightly larger ionic radius of doped Sn^{4+} (0.069 nm) compared to Ti^{4+} (0.0606 nm). Another indication for the substitution of Ti^{4+} atoms by the dopant in the crystal structure is a slight increase of the d-spacing of 0.345 nm (TiO$_2$), 0.347 nm (Ti$_{0.94}$Sn$_{0.06}$O$_2$), 0.349 nm (Ti$_{0.89}$Sn$_{0.11}$O$_2$) and 0.353 nm (Ti$_{0.85}$Sn$_{0.15}$O$_2$), which is consistent with the (101) planes of a tetragonal-phase anatase. The BET surface areas of the samples decreased with higher Sn doping content [TiO$_2$ (245 m^2 g^{-1}), Ti$_{0.94}$Sn$_{0.06}$O$_2$ (230 m^2 g^{-1}), Ti$_{0.89}$Sn$_{0.11}$O$_2$ (208 m^2 g^{-1}), and Ti$_{0.85}$Sn$_{0.15}$O$_2$ (178 m^2 g^{-1})] corresponding to an increase of the average crystallite size with more Sn, which was confirmed via TEM images (see Fig. 3a−c.) [8]. The average crystallite size (sampled from the size of 150 crystals) increased with higher Sn doping, from *ca.* 4.0 nm for pure TiO$_2$, to *ca.* 5.4 nm for Ti$_{0.85}$Sn$_{0.15}$O$_2$.

EDX measurements suggested Ti:Sn ratios for the samples of 94:6 Ti$_{0.94}$Sn$_{0.06}$O$_2$, 89:11 for Ti$_{0.89}$Sn$_{0.11}$O$_2$ and 85:15 for Ti$_{0.85}$Sn$_{0.15}$O$_2$. X-Ray photoelectron spectroscopy (XPS) analysis of the as-prepared Ti$_{0.85}$Sn$_{0.15}$O$_2$ sample is presented in Fig. 3e−f. For each sample, the ratio of Ti to Sn was investigated with the high-resolution Ti 2p and Sn 3d spectra. The high-resolution spectrum of Ti 2p showed binding energies for Ti 2p$_{3/2}$ at 458.16 and Ti 2p$_{1/2}$ at 463.97 eV, which were assigned to Ti^{4+} in TiO$_2$ [17]. The high-resolution XPS spectrum of Sn 3d, showed peaks corresponding to the binding energies for Sn 3d$_{5/2}$ at 486.4 and Sn 3d$_{3/2}$ at 494.8 eV, which were assigned to Sn^{4+} [18]. According to the XPS data, the
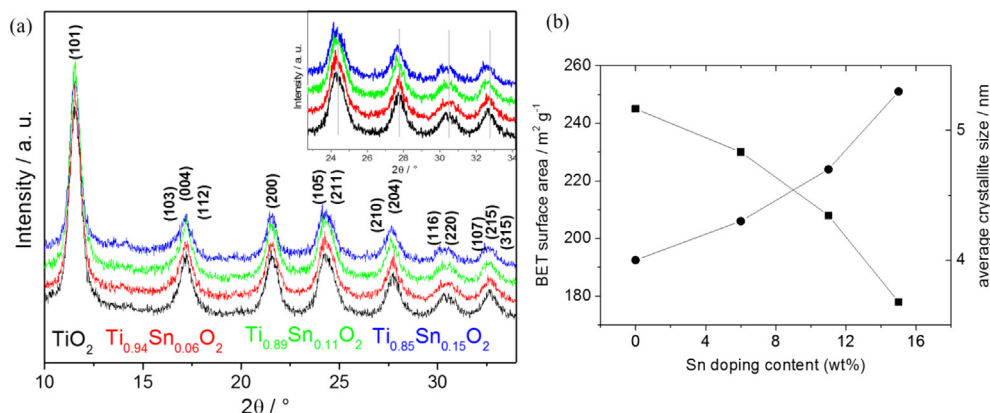
Fig. 2. (a) The XRD patterns of undoped anatase TiO_2, $Ti_{0.94}Sn_{0.06}O_2$, $Ti_{0.89}Sn_{0.11}O_2$ and $Ti_{0.85}Sn_{0.15}O_2$. (b) BET surface area and average crystallite size determined via TEM, versus the doping amount of Sn in the TiO_2 which was determined by EDX.
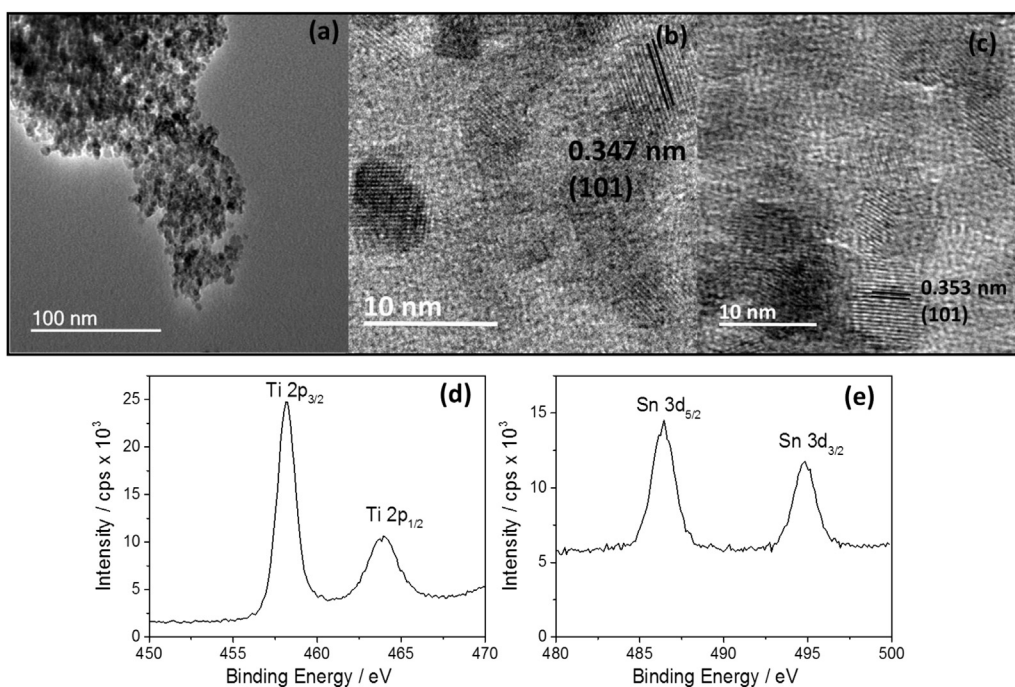

Fig. 3. The TEM images of (a) undoped anatase TiO_2, (b) $Ti_{0.89}Sn_{0.11}O_2$ and (c) $Ti_{0.85}Sn_{0.15}O_2$. XPS spectra for the $Ti_{0.85}Sn_{0.15}O_2$ sample: high-resolution (d) Ti 2p and (e) Sn 3d spectra.

doping content x of tin in $Ti_{1-x}Sn_xO_2$ increased with higher tin loading: $Ti_{0.94}Sn_{0.06}O_2$ (suggested as 11.5%), $Ti_{0.89}Sn_{0.11}O_2$ (suggested as 18.8%), $Ti_{0.85}Sn_{0.15}O_2$ (suggested as high as 26.5%). These differences are understandable when one considers that XPS is a surface technique and given that these Sn doped phases are metastable forms and possess very high surface areas, it is highly likely that the larger Sn^{4+} cations prefer to be nearer to the surface of these very small crystallites. Therefore, XPS and EDX measurements suggested successful incorporation of Sn^{4+} into the nanoparticles, with the actual Sn at% increasing as the concentration of the Sn precursor was increased during the synthesis.

Cyclic voltammetry (CV) measurements at a scan rate of 0.05 mV s^{-1} in the range of 0.05–3 V vs Li/Li$^+$, are presented in Fig. 4. A pair of cathodic and anodic peaks were observed in the potential range 1.5 and 2.3 V vs Li/Li$^+$, relating to Li-ion insertion into and extraction from the interstitial octahedral site of TiO_2 (see equation (1)). Under normal circumstances, a two-phase reaction is

expected to occur during lithiation with phase equilibrium of the Li-poor $Li_{0.01}TiO_2$ (tetragonal) phase and the Li-rich $Li_{0.55}TiO_2$ (orthorhombic) phase [19,20]. The detected specific current peak decreased with higher amount of Sn, thereby reducing the amount of pure TiO_2. The pure TiO_2 sample showed virtually no electrochemical activity in the potential range between 1.3 and 1 V vs Li/Li$^+$ during the first cycle. The increasing specific current during the first cycle between 1 and 0.05 V vs Li/Li$^+$, is attributed to solid electrolyte interface (SEI) formation (electrolyte destruction) at lower potentials [13]. There was also likely to be substantive SEI formation at the crystallite surfaces of the Sn-doped materials compared to the undoped TiO_2, as there was significant electrochemical activity in the range of 1.3 to 1 V vs Li/Li$^+$ for the former. However, as the surface area decreases with higher Sn-loading, the initial capacity loss due to the SEI formation may be expected to decrease. The general trend in fact showed that with higher Sn-loading, the initial irreversible capacity loss increased (from
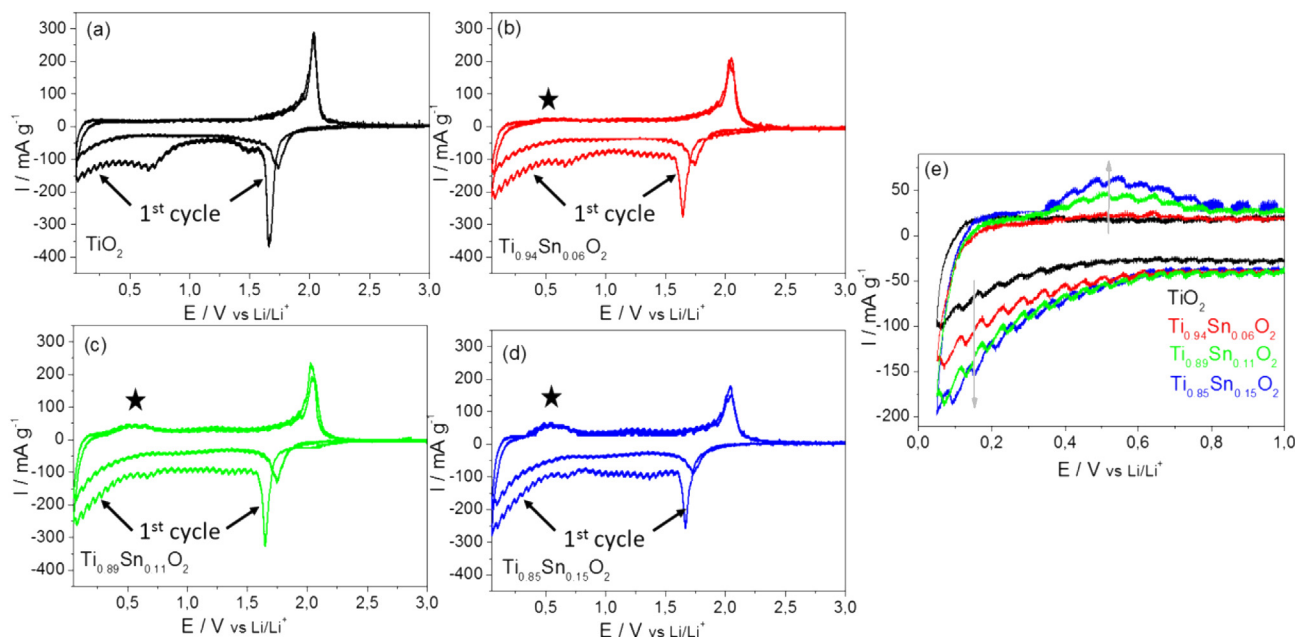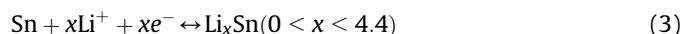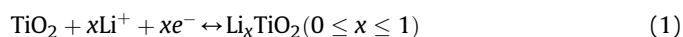
Fig. 4. Cyclic voltammograms for the 1st and 2nd cycles for the as-prepared nano-powder in the potential range of 0.05 and 3 V vs. Li/Li$^+$ for an applied scan rate of 0.05 mV s^{-1} for (a) undoped anatase TiO$_2$, (b) Ti$_{0.94}$Sn$_{0.06}$O$_2$, (c) Ti$_{0.89}$Sn$_{0.11}$O$_2$, and (d) Ti$_{0.85}$Sn$_{0.15}$O$_2$. (e) Specific current versus potential of the 2nd cycle for all materials at lower potentials. The specific current was calculated by taking into account the active material mass loadings.

363 mAh g^{-1} for the pure TiO$_2$ and 467 mAh g^{-1} for Ti$_{0.85}$Sn$_{0.15}$O$_2$).

The CVs herein and literature, suggest a plausible explanation for reaction chemistry of the Sn in the doped anatase nano-materials. The effect of electrochemically active Sn-dopants in TiO$_2$ was also investigated previously. Wang et al. investigated meso-porous Sn-doped TiO$_2$ thin films as anode materials. They showed that 6 at% Sn could be doped into the TiO$_2$ and although the Sn was doped in the structure, the Sn remained active in the same potential ranges (1–0.05 V for lithiation and 0.5 V for delithiation), which also contributed to a higher irreversible capacity loss during the first cycle and higher capacities during cycling, e.g. compared to the pure TiO$_2$ (101 mAh g^{-1}) the doped material exhibited a specific capacity of 253 mAh g^{-1} at an applied current of 85 mA g^{-1} [21]. The same behaviour was shown for literature reports on tin titanate nanotubes, where a synergistic effect of combining the advantages of "TiO$_2$" in terms of cycle life and "SnO$_2$" in terms of specific capacity, was observed [22]. For a 27 at% Sn-doped TiO$_2$, a specific capacity of 240 mAh g^{-1} was obtained over 300 cycles (compared to 168 mAh g^{-1} of the pure TiO$_2$) at an applied current of 250 mA g^{-1} [22]. Both these reports included CV measurements, which showed high current peaks at low potentials (0–0.5 V vs Li/Li$^+$), which was due to the formation of Li$_{4.4}$Sn, and a characteristic peak at 0.5 V vs Li/Li$^+$ for the delithiation of the alloy. Therefore, the authors suggest that during the first reduction cycle (at low potential) the Sn^{4+} in the anatase structure is reduced to a separate phase of elemental tin (Sn^0) with Li$_2$O being irreversibly formed (as suggested in a report by Wang et al.[23] and which could be one reason for the higher irreversible capacity loss). This is shown in equation (2) below. At lower potentials, this Sn^0 was then lithiated in the range 1.0 to 0.05 V vs Li/Li$^+$. Therefore, moving to lower potentials most likely favours the formation of Li$_x$Sn alloy (where 0 < x ≤ 4.4), see equation (3) [24,25]. The high volume expansion during lithiation to its metallic state, followed by more volume expansion during lithiation of the Sn metal forming an alloy, is expected to be >200% [23,26]. Therefore, it can be suggested that the elemental Sn then behaves thereafter, like a separate Sn alloy material phase. Delithiation of the samples in the potential range

0.05–3 V vs Li/Li$^+$ (forward sweep in the CV) showed a broad oxidation peak at 0.5 V for, which the specific current response increased with higher Sn at%. This appears to be due to the deli-thiation of the Li$_x$Sn (i.e. the back reaction of equation (3) below). Thus, after the first cycle, the authors suggest that these doped materials might form a nanocomposite of Sn and TiO$_2$ in the cell, which allows buffering of the higher specific capacity Sn (largely active below 1.0 V vs Li/Li$^+$) with the less expansive TiO$_2$ (active in the range of *ca.* 1.0–3.0 V vs Li/Li$^+$).

$$TiO_2 + xLi^+ + xe^- \leftrightarrow Li_xTiO_2 (0 \leq x \leq 1) \tag{1}$$

$$SnO_2 (\text{doped in the titania}) + 4Li^+ + 4e^- \leftrightarrow Sn + 2Li_2O \tag{2}$$

$$Sn + xLi^+ + xe^- \leftrightarrow Li_xSn (0 \leq x \leq 4.4) \tag{3}$$

Whilst the energy density of the battery is the product of the specific capacity and the overall cell voltage, power density is the measure of the rate that energy can be stored and released from a system. A high power electrode material has to possess high solid-state ion diffusivity, high electrical conductivity, minimized solid-state path lengths for ion transport, rapid electron transport and finally, a high electrode/electrolyte surface area [9]. According to this, small crystallite sizes and high surface areas, favour high power performance of electrode materials. Nano-TiO$_2$ crystallites used herein, had a crystallite size of ca. 4 nm and a BET surface area of 245 m^2 g^{-1}. The total amount of stored charge for such high surface area metal oxides can be separated into the faradaic contribution of the Li$^+$ ion insertion process as well as pseudoca-pacitance (charge-transfer process with surface atoms) and non-faradaic contributions from Helmholtz double layer charging. Wang et al. reported an increase of stored charge via pseudocapacitance and a decrease of stored Li$^+$ ions inserted into the structure at higher applied current rates. This effect was shown to increase with reduced crystallite size and higher surface area [27]. In Fig. 5, a scan rate test is presented. The linear relationship of the cathodic and anodic peak current i_p versus the square root of the scan rate $v^{1/2}$
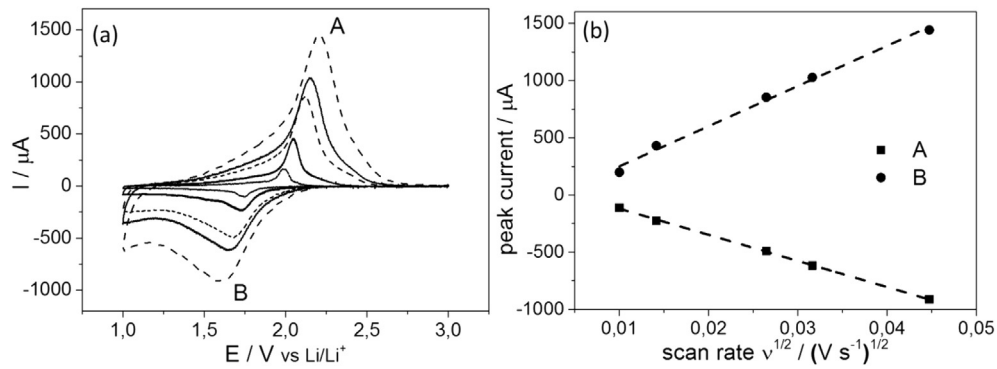
Fig. 5. Scan rate test for the pure TiO_2 material: (a) CV profiles at an applied scan rate of 0.1, 0.2, 0.7, 1 and 2 mV s^{-1} in the range 1–3 V vs. Li/Li$^+$. (b) Relationship between the peak current of the CV profile and the square root of the scan rate.

indicates a lithium diffusion limited process. The diffusion coefficient can be calculated with the Randles−Sevcik equation [28−30] (equation (4)), where i_p is the peak current in amps, n is the charge transfer number, A is the contact area between the electrolyte and the active material (geometric area as approximation 2.011 cm^2), c_{Li} is the maximum concentration of Ti^{3+} in the lattice, i.e., 0.024 mol cm^{-3} for $x = 0.5$ in Li$_x$TiO$_2$ [31]. D_{Li} is the chemical diffusion coefficient for Li$^+$ in cm^2 s^{-1}, which was calculated for sweep rates between 0.1 and 2 mV s^{-1}.

$$i_p = \left(2.69 \cdot 10^5\right) n^{3/2} A\, c_{Li}\, \nu^{1/2}\, D_{Li}^{1/2} \qquad (4)$$

The diffusion coefficient was ca. 2.4· 10^{-16} cm^2 s^{-1} for the lithiation and 5.3· 10^{-16} cm^2 s^{-1} for the delithiation. Sn-doped TiO$_2$ did not show a significant trend for the diffusion coefficient with higher Sn-loading [e.g. for the lithiation: 4.5· 10^{-16} cm^2 s^{-1} (Ti$_{0.94}$Sn$_{0.06}$O$_2$), 1.8· 10^{-16} cm^2 s^{-1} (Ti$_{0.89}$Sn$_{0.11}$O$_2$), 2.1· 10^{-16} cm^2 s^{-1} (Ti$_{0.85}$Sn$_{0.15}$O$_2$)]. In general, the reported lithion-ion diffusion coefficients for titanates vary from 10^{-9} cm^2 s^{-1} to 10^{-17} cm^2 s^{-1}. However, the diffusion coefficients herein are comparable to reported values of high surface area nano-TiO$_2$ in literature [27,32−34].

The pure anatase TiO$_2$ crystallites were cycled galvanostatically at an applied current ranging from 0.1 A g^{-1} which is *ca.* C/2, (as 1C = 170 mA g^{-1}) to 10 A g^{-1}, which is *ca.* 60 C, in the potential range 1−3 V vs Li/Li$^+$ (see Fig. 6). The irreversible capacity loss during the first cycle was always lower than 35 mAh g^{-1} @ 0.1 A g^{-1}. Compared to the existing and reported TiO$_2$ crystallites in literature, the nano-TiO$_2$ herein, showed excellent performance. For example, Han et al. investigated the high power rate capability of

TiO$_2$ nanotubes, directly grown on the current collector and randomly orientated. The directly grown TiO$_2$ nanotubes showed very high rate capability with >130 mAh g^{-1} at 20 C, which can be attributed to low resistance between the active material and the current collector. Keeping in mind that the synthesis was via a thin film method resulting in lower energy density, the randomly orientated nanotubes with the same ratio of active mass to conductive carbon as additive (70:20:10 active:carbon additive:-binder), only gave a specific capacity of 48 mAh g^{-1} at 3.35 A g^{-1} [35]. Chen et al. synthesized ultrathin anatase nanosheets in several steps, including an autoclave step for 24 h, followed by two heat-treatments. This gave crystallites with a specific surface area of 170 m^2 g^{-1} (TiO$_2$ herein was 245 m^2 g^{-1}). In that work, a capacity of *ca.* 95 mAh g^{-1} was achieved at the highest applied constant current of 3.35 A g^{-1} [36]. In contrast, the TiO$_2$ crystallites generated by the CHFS reactor herein, gave a specific capacity of 88 mAh g^{-1} at 5 A g^{-1} and 70 mAh g^{-1} at 10 A g^{-1}. In comparison, Wang et al. reached a reversible capacity of 98 mAh g^{-1} at an applied constant current of *ca.* 5 A g^{-1} for self-assembled TiO$_2$-graphene nanostructures, synthesized via co-precipitation and heat-treatment [37]. Lei et al. used a four-step synthesis to make nano-TiO$_2$ hollow spheres with a capacity of *ca.* 100 mAh g^{-1} at 1.67 A g^{-1} [38]. Herein, at an applied current of 2 A g^{-1}, the undoped 4 nm TiO$_2$ still possessed a capacity of 105 mAh g^{-1}. Chen et al. synthesized Ti^{3+} doped TiO$_2$ via a solvothermal batch method and suggested that the Ti^{3+} increased electronic conductivity, resulting in an improved rate performance with a capacity of 81 mAh g^{-1} at an applied current of 3 A g^{-1} [39]. Recently, it has been reported that rutile TiO$_2$ can exhibit good rate capability [32,40]. Hong et al. investigated self-assembled nanoporous rutile TiO$_2$ mesocrystals, which
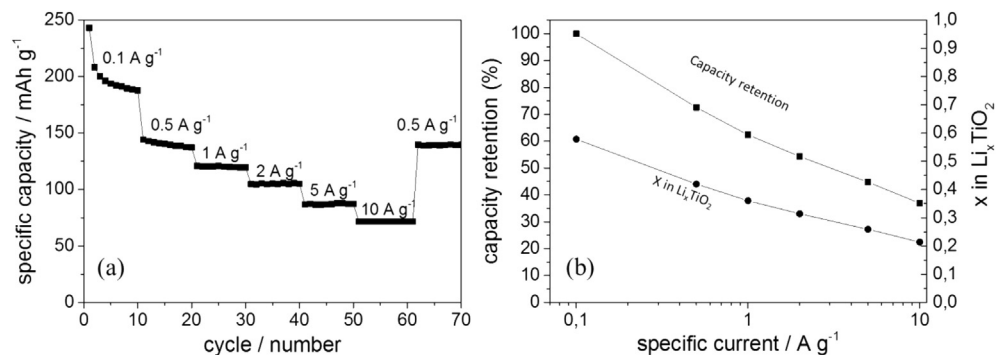

Fig. 6. (a) Plot of specific capacity (y-axis) versus cycle number (10 cycles at each rate) for the undoped nano-TiO$_2$ at different current rates. The material was cycled in the range of 1−3 V vs. Li/Li$^+$. (b) Capacity retention (left y-axis, squares) and the amount x of stored lithium in Li$_x$TiO$_2$ (right y-axis, circles) versus the specific applied current. The capacity at the 3rd cycle at 0.1 A g^{-1} was set as 100% for the capacity retention.

retained a capacity of 77 mAh g^{-1} at an applied current of 3.4 A g^{-1} [41]. Qiu et al. investigated hydrogenated rutile TiO$_2$ nanoparticles (synthesized by treating rutile TiO$_2$ with hydrogen at high pressure and temperature). The material retained an excellent specific capacity of 130 mAh g^{-1} at a current rate of 1.7 A g^{-1} [42]. Usui et al. used Nb-doped rutile TiO$_2$ (synthesized by a sol−gel method followed by heat-treatment steps) as a Li-ion battery anode. This electrode attained an impressive rate capability, with a capacity of 120 mA h g^{-1} at the highest applied current density of 16.75 A g^{-1}. The improvements in the performances are attributed to three orders of magnitude higher electronic conductivity of Ti$_{0.94}$Nb$_{0.06}$O$_2$ compared to that of pure TiO$_2$ [43]. Considering all these comparisons, the TiO$_2$ materials reported herein were made directly using a single step process in water (and using inexpensive precursors), which is a much more convenient approach compared to other more cost-, time- and energy-intensive synthesis routes that are often reported in the literature. Herein, the high surface area of our anatase material was also thought to increase the stored charge capacity via pseudocapacitance and double layer capacitance of the anode materials.

The influence of Sn-doping on the electrochemical performance was investigated via C-rate and long-term measurements in the range 1−3 V vs. Li/Li$^+$ (Fig. 7a and b). The results show that with increasing Sn-doping (and therefore, with relatively less of the active TiO$_2$ in this potential range), the overall specific capacity decreased as might be expected. Considering the decrease in surface area and increase of crystallite size, the C-rate retention did not benefit from Sn-doping, because a larger crystallite size could be expected to decrease ionic diffusion (conductivity), and limit the material as a high power anode. The same trend was observed for the long-term charge/discharge cycling tests at an applied current of 300 mA g^{-1} (range of 1−3 V vs Li/Li$^+$). With a greater amount of Sn-doping, the specific capacity decreased, whereas the stability was generally very high (91% capacity retention after 300 cycles to

give a final value of 165 mAh g^{-1} for the undoped nano-TiO$_2$ at a current rate of 300 mA g^{-1}). In comparison, the Sn doped samples at an applied current of 300 mA g^{-1} (range of 1−3 V vs Li/Li$^+$) showed a similar steady retention of their initial capacities, albeit lower than the sample with the most titania (Fig. 7b).

After the initial tests, the potential window was widened down to 0.05 V vs Li/Li$^+$. The main benefit from this was in the likely electrochemical activation of the Sn doped in the anatase, which thereafter was expected to form a separate phase after the initial activation. In the variable C-rate tests (as shown in Fig. 7c), greater Sn-doping increased the specific capacity. At an applied current of 100 mA g^{-1} (in the C-rate tests) the Ti$_{0.85}$Sn$_{0.15}$O$_2$ sample showed a steady capacity loss with an average capacity of ca. 350 mAh g^{-1} (for first 10 cycles in the variable C rate tests as shown in Fig. 7a). Fig. 7d shows the results from the constant rate cycling of the materials (fixed current rate of 382 mA g^{-1}) in the wider potential range 0.05−3 V vs Li/Li$^+$. Interestingly, all the samples bar the one with the highest Sn loading, showed a steady capacity fade from initial values near to >200 mA g^{-1} for the doped samples, down to below 50 mA g^{-1} after 300 cycles (Fig. 7d). However, the sample with the highest Sn loading (starting from ca 270 mAh g^{-1}), showed a steady loss of capacity for the first 100 cycles, down to just over 200 mAh g^{-1} and then recovered back up to almost its initial value by ca 400 cycles, after which it was slowly fading again by 500 cycles (Fig. 7d). However, the anode had still retained a specific capacity of >200 mAh g^{-1} after 500 cycles. In comparison, mesoporous C−TiO$_2$−SnO$_2$ nanocomposites (co-assembly method followed by two heat-treatment steps) have been reported to possess a capacity of 300 mAh g^{-1} at an applied current of only 30 mA g^{-1} [44], and tin titanate nanotubes (ion-exchange synthesis under hydrothermal conditions followed by heat-treatment) were reported to have a capacity of 348 mAh g^{-1} at an applied current of 250 mA g^{-1} [22]. Co$_3$O$_4$-coated TiO$_2$ nanotubes (synthesized via electrochemical anodizing method followed by a heat-treatment
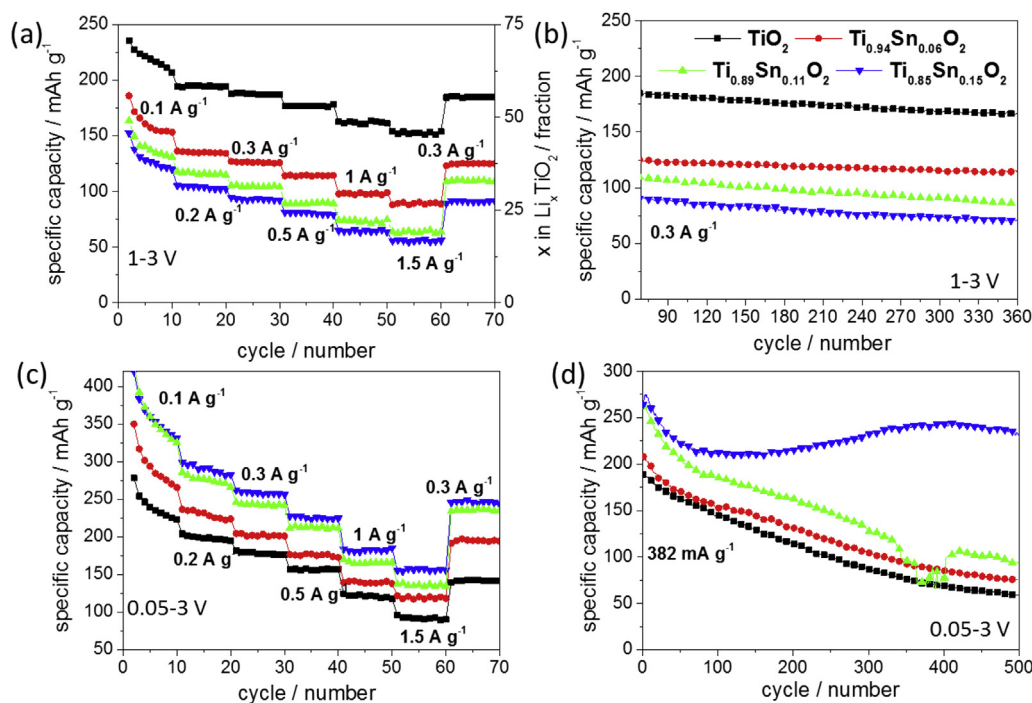

Fig. 7. Plots of specific capacity (left y axis) versus cycle number. (a) Variable current rate tests of all samples in the potential range between 1 and 3 V vs. Li/Li$^+$ (b) constant rate (charge/discharge) cycling tests in the potential range between 1 and 3 V vs. Li/Li$^+$ for all samples (c) Variable current rate tests of all samples in the potential range between 0.05 and 3 V vs. Li/Li$^+$, (d) constant rate (charge/discharge) cycling tests in the potential range between 0.05 and 3 V vs. Li/Li$^+$ for all samples (1st cycle not shown for c and d).
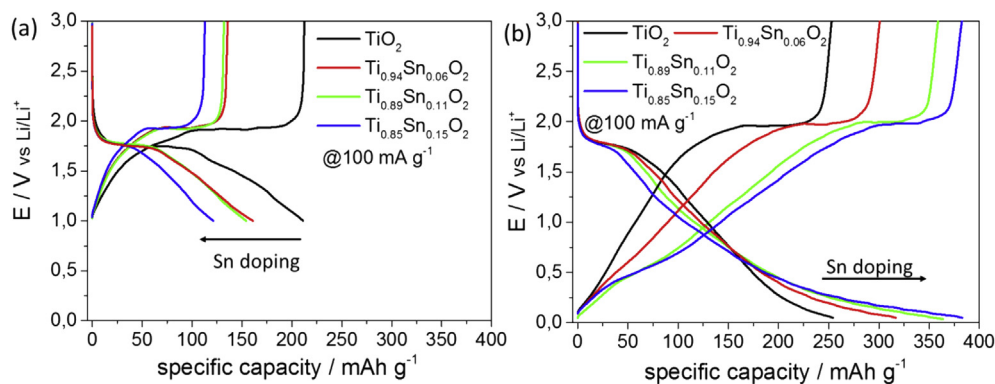
Fig. 8. Potential versus specific capacity plots for nano-TiO$_2$ and the Sn-doped titania at a constant applied current of 100 mA g^{-1} (a) in the potential range of 1–3 V vs Li/Li$^+$ and (b) in the potential range of 0.05–3 V vs Li/Li$^+$.

step) showed a reversible capacity of around 400 mAh g^{-1} at an applied current of 40 mA g^{-1} [45]. Usui et al. investigated composites of rutile-type TiO$_2$ and Si, which were synthesized by a facile sol–gel method. The binder-free composite electrodes exhibited very high cycle stability >900 cycles and a specific capacity of 710 mAh g^{-1} [46]. The latter two systems are of course not containing any Sn but show that a mixture of high capacity (e.g. Si) and low capacity (titania based) materials in such a way can be useful for giving both stable and high capacity anodes. The summary of the electrochemical performance of Sn-doped TiO$_2$ can be seen in Fig. 8. In the potential range 1–3 V vs Li/Li$^+$, the tin remains electrochemically inactive and does not appear to contribute to the stored charge of the anode. If the potential window is widened to be in the range 0.05 V–3 V vs Li/Li$^+$, the tin dopant drastically improves the electrochemical capacity of the anode through additional charge storage at lower potentials.

4. Conclusions

Pure anatase nano-TiO$_2$ crystallites were directly synthesized using a CHFS reactor, and with no further processing of the dried powders, the materials were made into printed anodes. The nanoparticles from CHFS showed excellent high power performances as a Li-ion battery anode up to an applied current of 10 A g^{-1} (*ca.* 60 C). The high surface area and low crystallite size contributed to the observed rate capability. Doping Sn into the anatase structure did not improve high power performance in the potential range 1–3 V vs Li/Li$^+$. However, if the potential range was widened to the range 0.05–3 V vs Li/Li$^+$, the Sn-dopant became electrochemically active and increased the overall capacity significantly. The wider operational window and the higher capacity of the doped materials, would be expected to increase the energy density in a full cell in the future. The simplicity of the synthesis process, offers good possibilities for scale-up of the synthesis to build full cells or larger cells in the future. Thus, the authors plan to investigate scale-up syntheses of these materials using a CHFS pilot plant process capable of producing nanomaterials at a rate >1 kg/h. The results from these endeavours, as well as larger scale cell manufacture and testing, will be reported in due course.

Acknowledgements

References

[1] R.I. Gruar, C.J. Tighe, J.A. Darr, Industrial Eng. Chem. Res. 52 (2013) 5270–5281.
[2] J.A. Darr, M. Poliakoff, Chem. Rev. 99 (1999) 495–542.
[3] H. Hayashi, Y. Hakuta, Materials 3 (2010) 3794–3817.
[4] T. Adschiri, Y. Hakuta, K. Sue, K. Arai, J. Nanoparticle Res. 3 (2001) 227–235.
[5] C.J. Tighe, R.Q. Cabrera, R.I. Gruar, J.A. Darr, Industrial Eng. Chem. Res. 52 (2013) 5522–5528.
[6] M. Chen, C.Y. Ma, T. Mahmud, J.A. Darr, X.Z. Wang, J. Supercrit. Fluids 59 (2011) 131–139.
[7] X. Lu, M. Yu, G. Wang, T. Zhai, S. Xie, Y. Ling, Y. Tong, Y. Li, Adv. Mater. 25 (2013) 267–272.
[8] Z. Zhang, S. Brown, J.B.M. Goodall, X. Weng, K. Thompson, K. Gong, S. Kellici, R.J.H. Clark, J.R.G. Evans, J.A. Darr, J. Alloys Compd. 476 (2009) 451–456.
[9] P.V. Braun, J. Cho, J.H. Pikul, W.P. King, H. Zhang, Curr. Opin. Solid State Mater. Sci. 16 (2012) 186–198.
[10] Y. Wang, H. Li, P. He, E. Hosono, H. Zhou, Nanoscale 2 (2010) 1294–1305.
[11] V. Etacheri, R. Marom, R. Elazari, G. Salitra, D. Aurbach, Energy & Environ. Sci. 4 (2011) 3243–3262.
[12] D. Deng, M.G. Kim, J.Y. Lee, J. Cho, Energy & Environ. Sci. 2 (2009) 818–837.
[13] W.-J. Zhang, J. Power Sour 196 (2011) 13–24.
[14] M.V. Reddy, G.V. Subba Rao, B.V.R. Chowdari, Chem. Rev. 113 (2013) 5364–5457.
[15] S. Goriparti, E. Miele, F. De Angelis, E. Di Fabrizio, R. Proietti Zaccaria, C. Capiglia, J. Power Sour 257 (2014) 421–443.
[16] M. Chen, C.Y. Ma, T. Mahmud, J.A. Darr, X.Z. Wang, J. Supercrit. Fluids 59 (2011) 131–139.
[17] G.S. Herman, Y. Gao, Thin Solid Films 397 (2001) 157–161.
[18] D. Barreca, S. Garon, E. Tondello, P. Zanella, Surf. Sci. Spectra 7 (2000) 81–85.
[19] J. Chen, L. Yang, Y. Tang, J. Power Sour 195 (2010) 6893–6896.
[20] J. Chen, L. Yang, Z. Zhang, S. Fang, S.-i. Hirano, Chem. Commun. 49 (2013) 2792–2794.
[21] Y. Wang, M. Xu, Z. Peng, G. Zheng, J. Mater. Chem. A 1 (2013) 13222–13226.
[22] H. Wang, L. Xi, J. Tucek, C. Ma, G. Yang, M.K. Leung, R. Zboril, C. Niu, A.L. Rogach, ChemElectroChem 1 (2014) 1563–1569.
[23] Y. Wang, Z.X. Huang, Y. Shi, J.I. Wong, M. Ding, H.Y. Yang, Sci. Rep. 5 (2015) 1–8 article no. 9164.
[24] C. Zhang, X. Peng, Z. Guo, C. Cai, Z. Chen, D. Wexler, S. Li, H. Liu, Carbon 50 (2012) 1897–1903.
[25] X. Zhu, Y. Zhu, S. Murali, M.D. Stoller, R.S. Ruoff, J. Power Sour 196 (2011) 6473–6477.
[26] G. Du, Z. Guo, P. Zhang, Y. Li, M. Chen, D. Wexler, H. Liu, J. Mater. Chem. 20 (2010) 5689–5694.
[27] J. Wang, J. Polleux, J. Lim, B. Dunn, J. Phys. Chem. C 111 (2007) 14925–14931.
[28] N. Tanaka, R. Tamamushi, Electrochimica Acta 9 (1964) 963–989.
[29] Z. Bi, M.P. Paranthaman, B. Guo, R.R. Unocic, H.M. Meyer III, C.A. Bridges, X.-G. Sun, S. Dai, J. Mater. Chem. A 2 (2014) 1818–1824.
[30] A.G. Dylla, G. Henkelman, K.J. Stevenson, Acc Chem. Res. 46 (2013) 1104–1112.
[31] L. Kavan, M. Grätzel, S.E. Gilbert, C. Klemenz, H.J. Scheel, J. Am. Chem. Soc. 118 (1996) 6716–6723.
[32] S. Kerisit, K.M. Rosso, Z. Yang, J. Liu, J. Phys. Chem. C 113 (2009) 20998–21007.
[33] M.L. Sushko, K.M. Rosso, J. Liu, J. Phys. Chem. C 114 (2010) 20277–20283.
[34] A.G. Dylla, J.A. Lee, K.J. Stevenson, Langmuir 28 (2012) 2897–2903.
[35] H. Han, T. Song, E.-K. Lee, A. Devadoss, Y. Jeon, J. Ha, Y.-C. Chung, Y.-M. Choi, Y.-G. Jung, U. Paik, ACS Nano 6 (2012) 8308–8315.

[36] J.S. Chen, Y.L. Tan, C.M. Li, Y.L. Cheah, D. Luan, S. Madhavi, F.Y.C. Boey, L.A. Archer, X.W. Lou, J. Am. Chem. Soc. 132 (2010) 6124—6130.
[37] D. Wang, D. Choi, J. Li, Z. Yang, Z. Nie, R. Kou, D. Hu, C. Wang, L.V. Saraf, J. Zhang, I.A. Aksay, J. Liu, ACS Nano 3 (2009) 907—914.
[38] J. Lei, W. Li, X. Li, E.J. Cairns, J. Mater. Chem. 22 (2012) 22022—22027.
[39] Y. Ren, J. Li, J. Yu, Electrochimica Acta 138 (2014) 41—47.
[40] Z. Hong, M. Wei, J. Mater. Chem. A 1 (2013) 4403—4414.
[41] Z. Hong, M. Wei, T. Lan, G. Cao, Nano Energy 1 (2012) 466—471.
[42] J. Qiu, S. Li, E. Gray, H. Liu, Q.-F. Gu, C. Sun, C. Lai, H. Zhao, S. Zhang, J. Phys.

[43] Chem. C 118 (2014) 8824—8830.
[43] H. Usui, S. Yoshioka, K. Wasada, M. Shimizu, H. Sakaguchi, ACS Appl. Mater. Interfaces 7 (2015) 6567—6573.
[44] Y. Zhou, C. Jo, J. Lee, C.W. Lee, G. Qao, S. Yoon, Microporous Mesoporous Mater. 151 (2012) 172—179.
[45] Y. Fan, N. Zhang, L. Zhang, H. Shao, J. Wang, J. Zhang, C. Cao, Electrochimica Acta 94 (2013) 285—293.
[46] H. Usui, K. Wasada, M. Shimizu, H. Sakaguchi, Electrochimica Acta 111 (2013) 575—580.